# The origin of the helicity hemispheric sign rule reversals in the mean-field solar-type dynamo

V.V. Pipin[1,2,3]⋆, H. Zhang[1]†, D.D. Sokoloff[1,4]‡, K.M. Kuzanyan[1,5]§, Y. Gao[1]¶

[1]*National Astronomical Observatories, Chinese Academy of Sciences, Beijing 100012, China*
[2]*Institute of Solar-Terrestrial Physics, Russian Academy of Sciences, Irkutsk, 664033, Russia*
[3]*Stanford University, Palo Alto, CA,..... U.S.A.*
[4]*Department of Physics, Moscow University, 119992 Moscow, Russia*
[5]*IZMIRAN, Russian Academy of Sciences, Troitsk, Moscow region 142190, Russia*

10 April 2013

**ABSTRACT**

Observations of proxies of the magnetic helicity in the Sun over the past two solar cycles revealed reversals of the helicity hemispheric sign rule (negative in the North and positive in the South hemispheres). We apply the mean-field solar dynamo model to study the reversals of the magnetic helicity sign for the dynamo operating in the bulk of the solar convection zone. The evolution of the magnetic helicity is governed by the conservation law. We found that the reversal of the sign of the small-scale magnetic helicity follows the dynamo wave propagating inside the convection zone. Therefore, the spatial patterns of the magnetic helicity reversals reflect the processes which contribute to generation and evolution of the large-scale magnetic fields. At the surface the patterns of the helicity sign reversals are determined by the magnetic helicity boundary conditions at the top of the convection zone. We demonstrate the impact of fluctuations in the dynamo parameters and variability in dynamo cycle amplitude on the reversals of the magnetic helicity sign rule. The obtained results suggest that the magnetic helicity of the large-scale axisymmetric field can be treated as an additional observational tracer for the solar dynamo.

**Key words:** Turbulence: Mean-field magnetohydrodynamics; Sun: magnetic field; Stars: activity – Dynamo

## 1 INTRODUCTION

Vector magnetographic observations of the solar active regions show that the distribution of the electric current helicity has a pronounced anti-symmetry with respect to the solar equator (Seehafer 1990; Pevtsov et al. 1994, 1995; Bao & Zhang 1998; Kuzanyan et al. 2000; Hagino & Sakurai 2005; Zhang et al. 2010). This phenomenon is called the hemispheric sign rule of current helicity. By analysis of the photospheric vector magnetograms of active regions it has been shown that the current helicity in the northern hemisphere is mainly negative while in the southern hemisphere it is positive. The same hemispheric sign rule was obtained from the synoptic magnetic field maps by Pevtsov & Latushko (2000) (see, also, Pevtsov et al. 2001). Both kinds of

observations deal with the line-of-sight part of current helicity, which can be identified with the total current helicity density using the assumption of the spatial isotropy of the current helicity distribution.

It is possible to relate the current helicity density with the magnetic helicity density taking into account the theoretical assumption on turbulent nature and isotropy of the magnetic fields (see, e.g., Moffatt 1978; Kleeorin & Rogachevskii 1999). Magnetic helicity is an integral of motion in MHD (Woltjer (1958); Moffatt (1969)). This impacts the saturation of the magnetic field generation in the large-scale helical dynamos (Frisch et al. 1975; Kleeorin & Ruzmaikin 1982; Vainshtein & Kitchatinov 1983; Kleeorin et al. 2000; Brandenburg & Subramanian 2005). Thus, the information about the surface distribution of the current helicity density and about its evolution with the solar cycle may be important for our understanding of the dynamo processes inside the solar convection zone (Kleeorin et al. 2003; Choudhuri et al. 2004; Zhang et al. 2012). It is also important for understanding the processes of the magnetic helicity transport

⋆ email: pip@iszf.irk.ru
† email: hzhang@bao.ac.cn
‡ email: sokoloff.dd@gmail.com
§ email: kuzanyan@gmail.com
¶ email: gy@bao.ac.cn

from the convection zone to the corona (Berger & Ruzmaikin 2000; Warnecke et al. 2011; Brandenburg et al. 2011).

The observations indicate departure from the hemispheric sign rule (Bao et al. 2000; Hagino & Sakurai 2005). It was found that at some periods of the solar cycle the hemispheric sign rule reverses to the opposite, at least at some latitudes and times (Zhang et al. 2010). It was realized that the properties of these reversals may be related with the kind of the dynamo operating in the Sun with the distribution of the dynamo processes inside the convection zone, and with the types of the magnetic helicity loss involved in the dynamo (see, e.g., Sokoloff et al. 2006; Guerrero et al. 2010; Mitra et al. 2011; Pipin & Kosovichev 2011b; Zhang et al. 2012). These mechanisms do not exclude the local processes which may take part in formation of the twisted magnetic field at the subsurface layers. Some of them were brought attention in the literature and could be considered as alternative points of view to the problem (see, e.g., Longcope et al. 1998; Kuzanyan et al. 2006; Pevtsov & Longcope 2007).

The purpose of this paper is to analyze the origin of the current helicity sign rule reversals within the framework of solar mean-field dynamo models. In our study we examine the dynamo distributed over the convection zone. In this model the global dynamo wave is shaped by the subsurface shear layer (Pipin & Kosovichev 2011c). Our approach is a development of the results of the dynamo model of (Pipin, Sokoloff, Zhang et al. 2013) which alleviates catastrophic quenching by consideration of total magnetic helicity conservation. We compare our results with that ones for the solar dynamo operating in overshoot layer at the bottom of the solar convective zone (see Zhang et al. 2012). Our study confronts the results of theoretical modeling with available observational data from Huairou Solar Observing Station of Chinese Academy of Sciences.

## 2    BASIC EQUATIONS

The details of the model can be found in our previous papers (see, e.g., Pipin et al. 2012; Pipin 2013 and Pipin 2008, hereafter P08). Here, we briefly outline the basic framework. We study the mean-field induction equation:

$$\frac{\partial \overline{\mathbf{B}}}{\partial t} = \boldsymbol{\nabla} \times \left( \boldsymbol{\mathcal{E}} + \overline{\mathbf{U}} \times \overline{\mathbf{B}} \right), \tag{1}$$

where $\overline{\mathbf{U}}$ is the mean velocity (differential rotation); $\overline{\mathbf{B}}$ is the axisymmetric magnetic field:

$$\overline{\mathbf{B}} = \boldsymbol{e}_\phi B + \boldsymbol{\nabla} \times \frac{A \boldsymbol{e}_\phi}{r \sin \theta}, \tag{2}$$

where $\theta$ is a polar angle and $r$ is a radial distance; $\boldsymbol{\mathcal{E}} = \overline{\mathbf{u} \times \mathbf{b}}$ is the mean electromotive force, with $\mathbf{u}$ and $\mathbf{b}$ are being the fluctuating velocity and magnetic field, respectively. Using the mean-field magnetohydrodynamic framework (Krause & Rädler 1980) we write the $\boldsymbol{\mathcal{E}}$ as follows:

$$\mathcal{E}_i = \left( \alpha_{ij} + \gamma_{ij}^{(\Lambda)} \right) \overline{B}_j - \left( \eta_{ijk} + \eta_{ijk}^{(\delta)} \right) \nabla_j \overline{B}_k, \tag{3}$$

where the turbulent kinetic coefficients are: the $\alpha$ effect, $\alpha_{ij}$; the turbulent pumping $\gamma_{ij}^{(\Lambda)}$; the anisotropic diffusivity $\eta_{ijk}$ and the $\delta$ dynamo effect (Rädler 1969), $\eta_{ijk}^{(\delta)}$. They depend

on the parameters of the turbulent convection, like the mean density and turbulent diffusivity stratification, the Coriolis number $\Omega^* = 2\tau_c \Omega_0$, where $\tau_c$ is the typical convective turnover time, and $\Omega_0$ is the global angular velocity.

The $\alpha$ effect includes the hydrodynamic and magnetic helicity contributions,

$$\alpha_{ij} = C_\alpha \sin^2 \theta \alpha_{ij}^{(H)} + \alpha_{ij}^{(M)}, \tag{4}$$

where the hydrodynamic part of the $\alpha$-effect is defined by $\alpha_{ij}^{(H)}$. The expressions for the turbulent kinetic coefficients $\alpha_{ij}^{(H)}$, $\gamma_{ij}^{(\Lambda)}$, $\eta_{ijk}$ and $\eta_{ijk}^{(\delta)}$ are given in Appendix. The contribution of small-scale magnetic helicity $\overline{\chi} = \overline{\mathbf{a} \cdot \mathbf{b}}$ ($\mathbf{a}$ is the fluctuating magnetic vector-potential) to the $\alpha$-effect is defined as follows (see, P08):

$$\alpha_{ij}^{(M)} = 2f_2^{(a)} \delta_{ij} \frac{\overline{\chi} \tau_c}{\mu_0 \overline{\rho} \overline{\ell}^2} - 2f_1^{(a)} e_i e_j \frac{\overline{\chi} \tau_c}{\mu_0 \overline{\rho} \overline{\ell}^2}. \tag{5}$$

The principal nonlinear feedback of the large-scale magnetic field to the $\alpha$-effect is due to a dynamical quenching because of the generation of the magnetic helicity by the dynamo (Frisch et al. 1975; Kleeorin & Ruzmaikin 1982; Brandenburg & Subramanian 2005). The relation of magnetic helicity on the large- and small scales (Hubbard & Brandenburg 2012; Pipin 2013) is governed by the equation:

$$\frac{\partial \overline{\chi}}{\partial t} = -\frac{\partial \left( \overline{\mathbf{A}} \cdot \overline{\mathbf{B}} \right)}{\partial t} - \frac{\overline{\chi}}{R_m \tau_c} - \eta \overline{\mathbf{B}} \cdot \overline{\mathbf{J}} - \boldsymbol{\nabla} \cdot \boldsymbol{\mathcal{F}}^\chi, \tag{6}$$

where $\boldsymbol{\mathcal{F}}^\chi = -\eta_\chi \boldsymbol{\nabla} \left( \overline{\chi} + \overline{\mathbf{A}} \cdot \overline{\mathbf{B}} \right)$ is the diffusive flux of the total magnetic helicity (Mitra et al. 2010), and $\eta_\chi$ is the turbulent diffusion coefficient for the magnetic helicity. In the paper we use $R_m = 10^6$ and $\eta_\chi = 0.1\eta_T$, where $\eta_T$ is the turbulent diffusivity profile (see, Appendix). For the axisymmetric magnetic fields the large-scale magnetic vector-potential is

$$\overline{\mathbf{A}} = \mathbf{e}_\phi T + \mathbf{r}P = \frac{\mathbf{e}_\phi}{r \sin \theta} A + r\mathbf{e}_r P. \tag{7}$$

The toroidal part of the vector potential is governed by the dynamo equations. The poloidal part of the vector potential can be restored from equation $\boldsymbol{\nabla} \times (\mathbf{r}P) = \mathbf{e}_\phi B$. We matched the potential field outside and the perfect conductivity at the bottom boundary with the standard boundary conditions. For the magnetic helicity we employ $\bar{\chi} = 0$ at the bottom of the convection zone. The paper elaborates two kind of the surface boundary conditions for the magnetic helicity:

$$\eta_\chi \nabla_r \left( \bar{\chi} + \overline{\mathbf{A}} \cdot \overline{\mathbf{B}} \right) \Big|_{r=r_e} = 0, \tag{8}$$

$$\eta_\chi \nabla_r \frac{\bar{\chi}}{(\overline{\rho} \ell^2)} \Big|_{r=r_e} = 0. \tag{9}$$

We call the model that satisfies the boundary conditions Eq. (8) as the model B1, and similar, the model B2 is referred to the Eq. (9). We set the seed magnetic field of the preferred dipole parity and with small admixture of the quadrupole one to check the parity preference when the solution reaches the steady state.

The construction of the radial profiles for the turbulent coefficients, which are involved in the mean electromotive force, remains rather arbitrary for various kinds of the dynamo models. In our models we use the solar convection zone model computed by Stix (2002). In the paper we use the same profiles for the turbulent coefficients as in our previous papers (see, Pipin 2013, and Appendix therein).
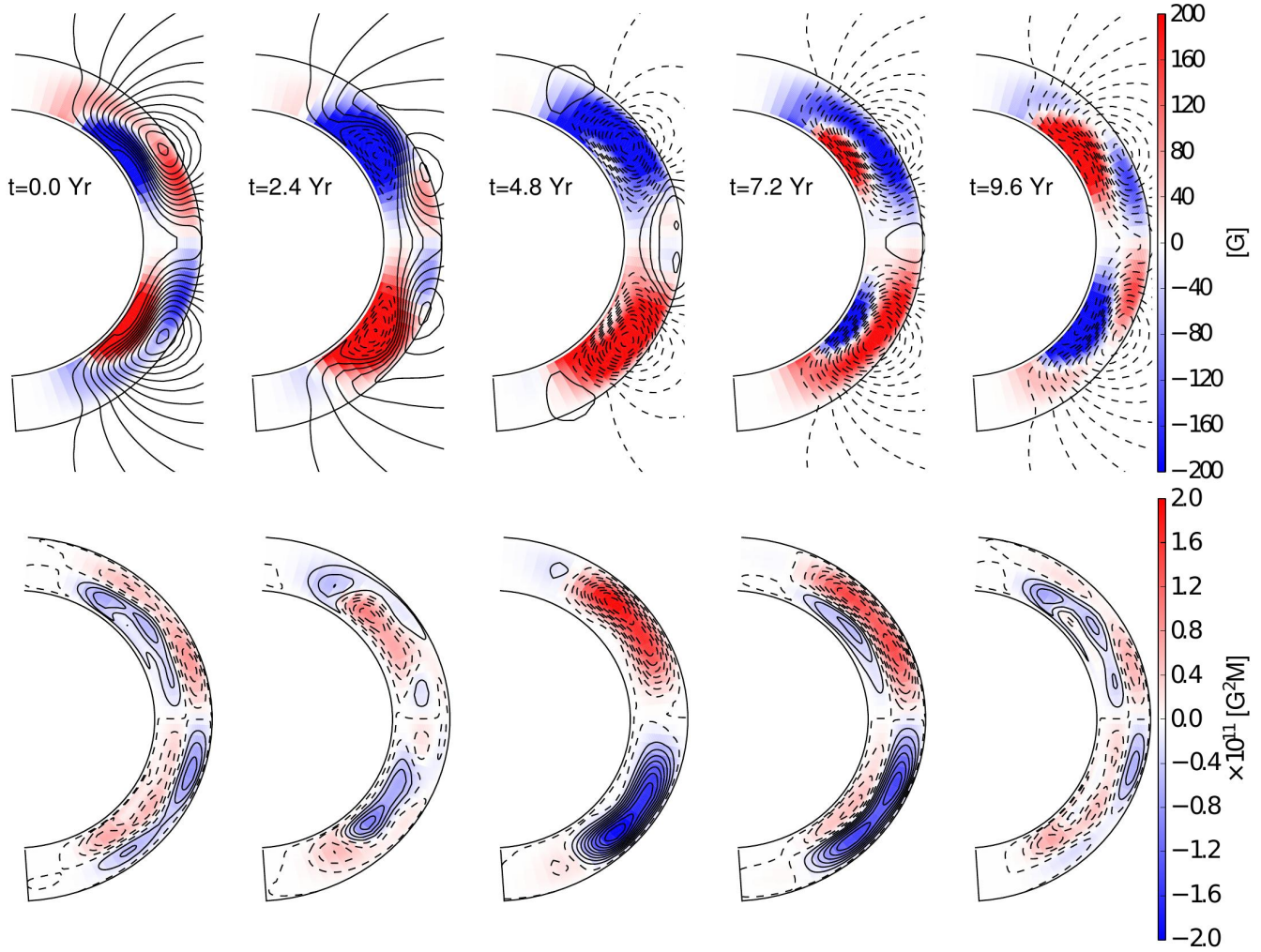
**Figure 1.** Snapshots of the magnetic field and magnetic helicity evolution inside the convection zone: Top panel shows the field lines of the poloidal component of the mean magnetic field and the toroidal magnetic field (varies $\pm 1$kG) is shown by color; Bottom panel shows the small-scale magnetic helicity density (contours) and the large-scale magnetic helicity density (color). Both quantities vary with the same magnitude.
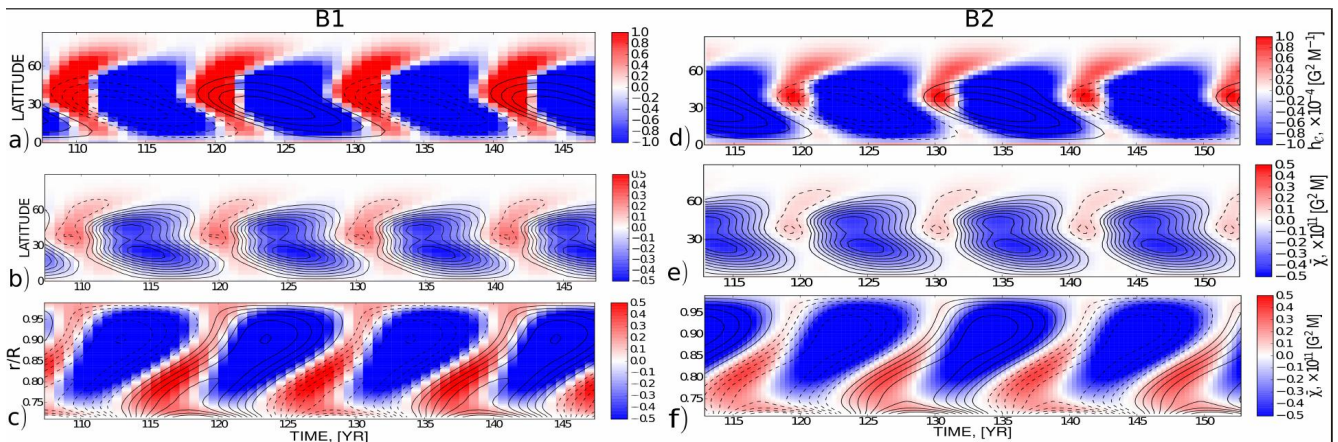


**Figure 2.** The left column shows the results for the model B1. Panel (a) shows the time-latitude diagram for the current helicity (background image). Panel (b) shows the toroidal magnetic field variations at $r = 0.95R$. panel (c) shows variations of the small-scale magnetic helicity and the toroidal magnetic field inside the convection zone at the latitude $30°$. Panels (d, e, f) show the same results for the model B2.

## 3   RESULTS

Fig. 1 shows the snapshots of the magnetic field and magnetic helicity evolution in the North hemisphere for the model B1 which uses Eq. (8). The qualitatively similar results can be obtained for the model B2. Here we see, that the spatial patterns of the small-scale magnetic field follow the evolution of the large-scale magnetic helicity and the latter propagates with the toroidal part of the dynamo wave from the bottom of the convection zone to the surface. The dynamo wave has the equatorial and the polar branches. Near the surface the equatorial branch dominates. The hemispheric helicity rule suggest that the small-scale helicity is negative at the North and positive at the South hemisphere. Fig. 1 shows that in the upper part of the convection zone the helicity rule is valid in the most phases of the cycle. In the upper part of the convection zone the reversal sign of the small-scale magnetic helicity regions appears at the high latitudes when the dynamo wave of the toroidal magnetic field comes to the subsurface shear layer. At the equatorial latitudes the reversal sign of $\overline{\chi}$ occurs at the decaying phases of the dynamo wave cycle. One can see that the signs of the large and small-scale helicities are spatially related. It is shown in Fig. 2 that shows the time-latitude and the time-radius variations of the magnetic field and magnetic helicity near the surface. The Figure also demonstrates the effect of the boundary condition change for the magnetic helicity. For the boundary condition Eq. (8) the regions with reversed sign of the small-scale magnetic helicity penetrate into the surface while the condition Eq. (9) quenches this penetration. We find that the patterns of the reversed sign of the magnetic helicity are located at the edges of the butterfly wings of the time-latitude diagrams for the large-scale toroidal magnetic field. The novel feature which is demonstrated by the Fig. 2 is the time-latitude diagram for the large-scale magnetic helicity which is attributed to the axisymmetric magnetic field. It is seen that within the current model its distribution is closely connected with the distribution of the small-scale helicity. It is believed that the current helicity of the surface magnetic field is the observational proxy for the magnetic helicity $\overline{\chi}$. We note that our model uses the full information about the large-scale magnetic helicity.

The difference in penetration of the magnetic helicity to the surface results in difference in the distribution of the effective $\alpha$ effect near the surface. This issue is recently discussed by Käpylä et al. (2012), Pipin, Sokoloff, Zhang et al. (2013) and Pipin (2013). Fig. 3 shows the snapshots of the $\alpha_{\phi\phi}$ and the small-scale magnetic helicity profiles for the different phase of the cycle at the latitude $45°$. We find that for the model B1 the $\alpha$-effect can be negative at the certain phases of the cycle and it has the sharp positive profile near the surface. The model B2 has the negative $\alpha$-effect for $r > 0.92R$ with the sharp negative profile near the surface. The abrupt growth of the $\alpha$ effect amplitude near the surface is because of the factor $\left(\overline{\rho}\ell^2\right)^{-1}$ in the definition, see Eq. (5). It remains the matter of the direct numerical simulations to justify the correct choice of the boundary condition for the magnetic helicity. The model B2 has the zero boundary condition for the derivative of the small-scale current helicity at the top, see Eq. 9. It is found that for the con-
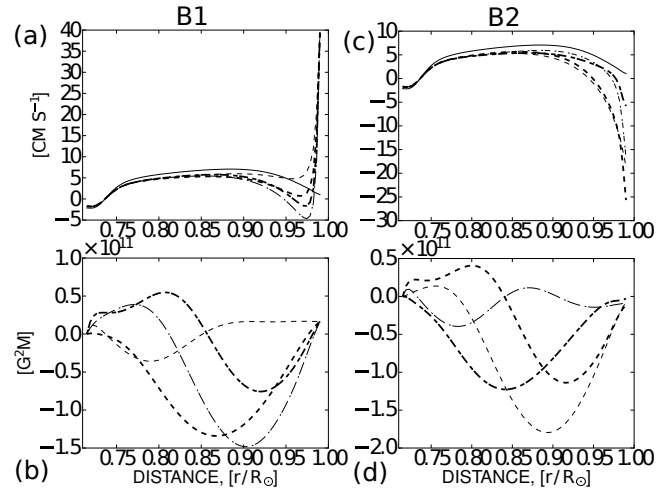


**Figure 3.** Panels (a,b) show variations of the $\alpha$-effect and the small-scale magnetic helicity at the latitude $45°$ for the model B1 (the Eq. (8)), and the panels (c,d) show the same for the model B2 (the Eq. (9)).

dition $\nabla_r\overline{\chi}|_{r\,=\,r_e} = 0$ the negative part of the alpha-effect near the surface is stronger than one in model B2.

### 3.1   Impact of dynamo fluctuations on the helicity patterns

The sign reversals of the helicity rule can be due to random fluctuations in the dynamo parameters and due to some random processes which generate the magnetic helicity independent of the large-scale dynamo. In this subsection we examine the effect of fluctuations in the dynamo parameters on the magnetic helicity distribution variations. We exploit here a scenario (Moss et al. 2008; Usoskin et al. 2009; Pipin et al. 2012) with fluctuations of $\alpha$-effect as a possible source of the solar activity cycle parameters from one cycle to another. We introduce random non-symmetric about equator variations of the $\alpha$-effect, $C_\alpha = C_\alpha \left(1 + 0.2 \left(\xi_N \Theta\left(\mu\right) + \xi_S \Theta\left(-\mu\right)\right)\right)$, where $\mu = \cos\theta$, $\Theta$ is the Heaviside function and $|\xi_{S,N}| < 2\sigma(\xi_{S,N})$ is the random Gaussian noise with the randomly floating phase and with the mean memory time equals to the dynamo cycle length. In this subsection the model B1 is discussed as it shows the stronger reversals of the helicity rule than the model B2.

We found that the reversals of the helicity rule are stronger during the periods of the grand minimum which are also related to the periods of the strong hemispheric asymmetry in the magnetic activity. Fig. 4 shows variations of the integral parameters of the model for the near surface magnetic field. In our results we show the parity index, that determines the symmetry of the toroidal magnetic field about equator, with the value $-1$ corresponds to the dipolar symmetry of the near surface toroidal magnetic fields and the value $1$ corresponds to the quadrupolar symmetry. The sunspot number was simulated in following to Pipin et al. (2012). We also show the integral magnetic helicity for each hemisphere. The magnitude of the helicity variations is in agreement with the observational constraints obtained by Berger & Ruzmaikin (2000). Variations of the magnetic helicity go in anti-phase at the large and small scales, be-
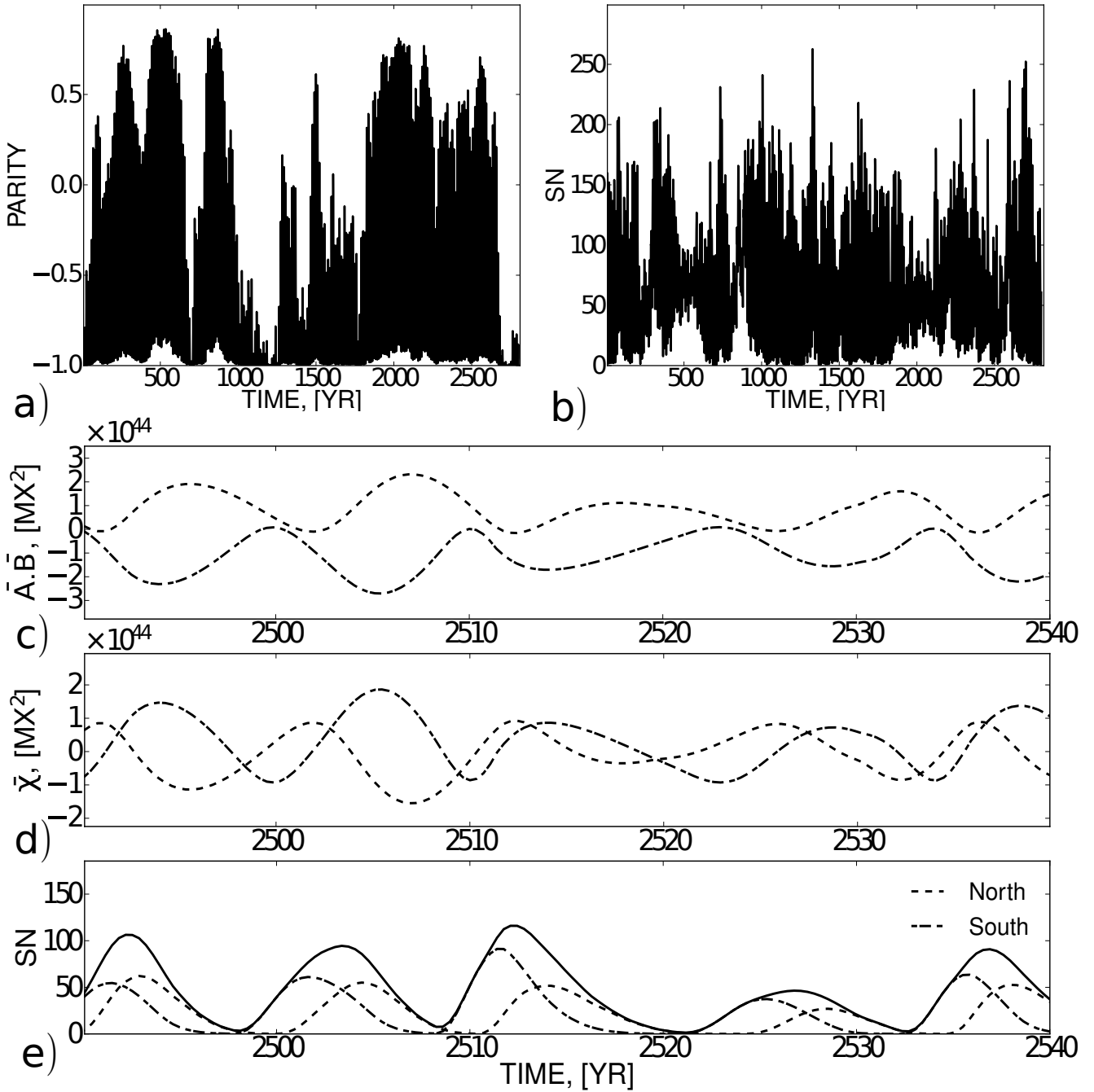
**Figure 4.** The integral characteristics of the magnetic activity near the surface, $r = 0.95R$ : a) the parity index determining the symmetry of the toroidal magnetic field about equator, -1 corresponds to the dipolar symmetry and 1 to the quadrupolar; b) the simulated sunspot number (SN); c) the latitudinal integral of the large-scale magnetic helicity, dashed line the North hemisphere, the dash-dotted line the South one; d) the same as (c) for the small-scale magnetic helicity; e) the same as (b), (the SN), the solid line is the total SN, the dashed line is the SN for the North hemisphere and the dash-dotted line is the SN for the South hemispere.

cause it is prescribed by Eq.(6). Nevertheless, for each hemisphere, there is a difference between the evolution of $\overline{\mathbf{A}} \cdot \overline{\mathbf{B}}$ and $\overline{\chi} = \overline{\mathbf{a} \cdot \mathbf{b}}$. The small-scale helicity, $\overline{\chi}$ does change the sign in a course of the solar cycle and the large-scale helicity $\overline{\mathbf{A} \cdot \mathbf{B}}$ almost does not. This is similar to results shown in Fig. 2, where we see that reversals of the helicity rule is much stronger for the small-scale helicity than for the large-scale one. Another interesting results is that the maxima of the

integral large-scale magnetic helicity are approximately corresponded to the maxima of the decay rate in the simulated sunspot activity (cf, Figs. 4c,d and Fig. 4e). This is due of the oscillatory character of the dynamo and delay between the activity of the major components of the large-scale magnetic fields which are related to the toroidal magnetic field and the large-scale toroidal vector-potential determining the poloidal magnetic field.

Finally, Fig. 5 shows comparison of the results for the simulated time-latitude diagrams for the toroidal magnetic field and the magnetic helicity with results of the current helicity observations reported by Zhang et al. (2010). We used systematic series of vector magnetographic observations of solar active regions by 35 cm filter type SMTF telescope at Huairou Solar Observing Station of Chinese Academy of Sciences. The data set comprises 6205 individual magnetograms of active regions more or less homogeneously covering the 18 year period of 1988-2005, which is almost two sunspot cycles. The data have been grouped and averaged into statistically significant sub-samples in time-latitudinal bins (2 years in time and 7 degrees in heliolatitude), see Zhang et al. (2010) for details. We have subsequently smoothed the data by using standard IDL linear interlopation for retaining only global features of the time-latitudinal distribution of helicity.

The results of the dynamo model are shown for the period of the grand minimum. It is the same period as discussed for the Fig. 4(c,d,e) above. The simulated butterfly diagrams are in visible qualitative agreement with the observations. One can see that the model keeps the basic anti-symmetry of helicity (negative in the North and positive in the South, i.e. the so-called hemispheric sign rule), however with evolution it shows various deviations from perfect periodicity (e.g., longer cycles, suppression of activity, asymmetry in the phases of growth and decay, asymmetry in the shape of wings on butterfly diagrams etc). It looks plausible that long and weak cycles are associated with larger areas of helicity of the sign opposite to the hemispheric sign rule.

## 4   DISCUSSION AND CONCLUSIONS

The available bulk of the current helicity data covers two activity cycles and the transition to the following activity cycle which has been quite unusual. The observed helicity butterfly diagrams demonstrate that the size of the areas with the opposite helicity signs in the later cycle differs substantially from the first one. We studied the origins of the reversals of the magnetic helicity sign in the mean-field solar dynamo. The evolution of the magnetic helicity in the model subject to the global constraint of the magnetic helicity conservation law. The nonlinear feedback of the large-scale magnetic field to the $\alpha$-effect is described by dynamical quenching due to the constraint of magnetic helicity conservation. The magnetic helicity, $\overline{\chi}$, is subjected to the conservation law.

In the model, the sign reversals of the small-scale magnetic helicity are always related with the sign reversals of the large-scale magnetic helicity. This is due to the magnetic helicity conservation constraint. The result develops the simple model by Xu et al. (2009). The idea was recently elaborated by Zhang et al. (2012) for the toroidal part of the current helicity. Our model employs the total large-scale magnetic helicity and not only its toroidal part. Taking into account Eqs.(2,7) we get the large-scale magnetic helicity formula for the spherical coordinates:

$$\overline{\mathbf{A}} \cdot \overline{\mathbf{B}} \quad = \quad \frac{A\,B}{r\sin\theta} + \frac{P}{r\sin\theta}\frac{\partial A}{\partial\theta}, \tag{10}$$

where, $B = \overline{B}_\phi = -\dfrac{\partial P}{\partial\theta}$ and $\overline{B}_r = \dfrac{1}{r^2\sin\theta}\dfrac{\partial A}{\partial\theta}$. We have to

notice that the magnetic helicity of the large-scale axisymmetric field can be restored from observational tracers of $\overline{B}_\phi$ and $\overline{B}_r$ either from the vector magnetograms Seehafer (1990) or from the line-of-sight magnetic observations, e.g., using method by Pevtsov et al. (2001). The toroidal part of the potential can be restored from the surface distribution of the $B_r$ as $A(\theta) = \int_0^\theta r^2 \sin\theta \overline{B}_r d\theta$ which is equivalent to the flux going outside of the Sun, and, similar, we can restore poloidal part of vector-potential using $P = -\int_0^\theta \overline{B}_\phi d\theta$. Note, that the total helisity remains zero because of the equatorial symmetry of the axisymetric magnetic field. Hence, the using of the Coulomb gauge is justified and the determination of the latitudinal distribution of the magnetic helicity of the axisymmetric large-scale magnetic fiel is unique.

Therefore, the observations can give an information about the magnetic helicity of the large-scale magnetic fields of the Sun. Our results indicate (see, Figs. 4(c,d,e) that the reversal of magnetic helicity and lower values of integral helicity may proceed the lower amplitude of cyclic dynamo activity.

We found that in the models the wave of the reversed magnetic helicity sign propagates from the bottom of the convection zone. Similar property was recently found by Warnecke et al. (2011) in direct numerical simulations. The models B1 and B2 show the possibility as for the strongly positive as well for the negative dynamical $\alpha$-effect near the top of the convection zone. The model employs the sub-surface rotational shear having the negative radial gradient of the angular velocity. Therefore, in case B1 the dynamo wave penetrates closer to equator than the model B2 because of the Parker-Yoshimura rule (Parker 1955; Yoshimura 1975). The numerical simulations demonstrate a similar effect (Käpylä et al. 2012).

Generally, the sign reversals of the magnetic helicity are stronger in the model B1 than in the model B2. These two models have different boundary conditions for the magnetic helicity at the top. In the model B1 the diffusive flux of the large-scale helicity from the surface is balanced by a counterpart from the small-scale helicity. Therefore, integrating the Eq. (8) from some level $r = r_0$ the top $r = r_e$ we have $\overline{\chi}_e = \overline{\chi}_0 + \overline{\mathbf{A}}_0 \cdot \overline{\mathbf{B}}_0$, where we use the magnetic boundary conditions as well. Thus, in the model B1, the boundary conditions support the penetration of the local helicity $\overline{\chi}_0 + \overline{\mathbf{A}}_0 \cdot \overline{\mathbf{B}}_0$ (governed by Eq. 6) from depth to the surface. For the boundary condition Eq. (9) we have $\nabla_r h_\mathcal{C} = 0$ at the top. This is the same as $\nabla_r \overline{\chi} = \overline{\chi}\Lambda(\bar\rho\ell^2)$, where $\Lambda(\bar\rho\ell^2) = \nabla_r \log(\bar\rho\ell^2)$. Thus, at the near surface level, in the model B2 the small-scale magnetic helicity is determined by the profile of $\Lambda(\bar\rho\ell^2)$ and not by Eq.(6). The further study requires clarification of the issue if the boundary conditions impact the sign reversals of the magnetic helicity. We can make conjecture that the change in the boundary conditions results in the larger or smaller sign reversals of the magnetic helicity at the surface.

The main results of the paper can be summarized as follows. The current model suggests that the reversal of the sign of the small-scale magnetic helicity follows the dynamo wave propagating inside the convection zone. This was also suggested by the numerical simulations (Warnecke et al. 2011). Therefore, the spatial patterns of the magnetic helicity reversals reflect the processes which contribute to generation and evolution of the large-scale magnetic fields. At the sur-
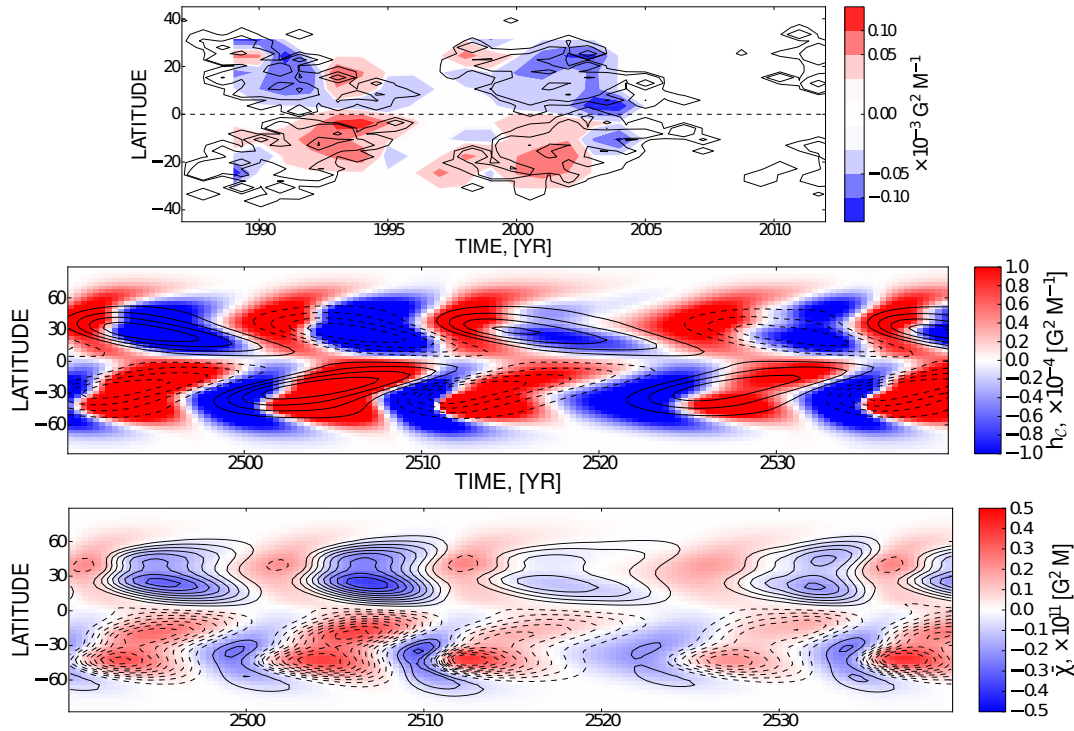
**Figure 5.** The time-latitude diagram for the current helicity as inferred from the solar active region observations at Huairou Solar Observing Station. Sunspot density which traces toroidal magnetic field is shown by colors while contour lines show current helicity, the vertical color bar on the right side scales the magnitude.

face the patterns of the helicity rule reversals are determined by the magnetic helicity boundary conditions at the top of the convection zone. The model suggests that the magnetic helicity of the large-scale axisymmetric field can be used as an additional observational tracer for the solar dynamo.

**REFERENCES**

Bao S., Zhang H., 1998, ApJ, 496, L43
Bao S. D., Ai G. X., Zhang H. Q., 2000, J. Astrophys. Astron., 21, 303
Berger M. A., Ruzmaikin A., 2000, J. Geophys. Res., 105, 10481
Brandenburg A., Subramanian K., 2005, Phys. Rep., 417, 1
Brandenburg A., Subramanian K., Balogh A. et al., 2011, ApJ, 734, 9
Choudhuri A. R., Chatterjee P., Nandy D., 2004, ApJL, 615, L57
Frisch U., Pouquet A., Léorat J. et al. 1975, J. Fluid Mech., 68, 769
Guerrero G., Chatterjee P., Brandenburg A., 2010, MNRAS, 409, 1619
Hagino M., Sakurai T., 2005, Publ. Astron. Soc. Japan, 57, 481
Hao J., Zhang M., 2011, ApJL, 733, L27
Hubbard A., Brandenburg A., 2012, ApJ, 748, 51
Käpylä P. J., Korpi M. J., Brandenburg A., 2008, A & A, 491, 353
Käpylä P. J., Mantere M. J., Brandenburg A., 2012, ApJL, 755, L22
Kleeorin N., Kuzanyan K., Moss D. et al. 2003, A & A, 409, 1097
Kleeorin N., Moss D., Rogachevskii I. et al. 2000, A & A, 361, L5
Kleeorin N., Rogachevskii I., 1999, Phys. Rev.E, 59, 6724
Kleeorin N. I., Ruzmaikin A. A., 1982, Magnetohydrodynamics, 18, 116
Krause F., Rädler K.-H., 1980, Mean-Field Magnetohydrodynamics and Dynamo Theory. B: Akademie
Kuzanyan K., Zhang H., Bao S., 2000, Solar Phys., 191, 231
Kuzanyan K. M., Pipin V. V., Seehafer N., 2006, Sol.Phys., 233, 185

Longcope D. W., Fisher G. H., Pevtsov A. A., 1998, ApJ, 507, 417

Mitra D., Candelaresi S., Chatterjee P. et al., 2010, Astron. Nachr., 331, 130

Mitra D., Moss D., Tavakol R. et al. 2011, A&A, 526, A138+

Moffatt H., 1969, J . Fluid Mech., 35, 117

Moffatt H. K., 1978, Magnetic Field Generation in Electrically Conducting Fluids. Cambridge, England: Cambridge University Press

Moss D., Sokoloff D., Usoskin I. et al. 2008, Solar Phys., 250, 221

Ossendrijver M., Stix M., Brandenburg A., 2001, A & A, 376, 713

Ossendrijver M., Stix M., Brandenburg A., et al 2002, A & A, 394, 735

Parker E. N., 1955, ApJ, 121, 491

Pevtsov A. A., Canfield R. C., Latushko S. M., 2001, ApJL, 549, L261

Pevtsov A. A., Canfield R. C., Metcalf T. R., 1994, ApJL, 425, L117

Pevtsov A. A., Canfield R. C., Metcalf T. R., 1995, ApJL, 440, L109

Pevtsov A. A., Latushko S. M., 2000, ApJ, 528, 999

Pevtsov A. A., Longcope D. W., 2007, in Shibata K., Nagata S., Sakurai T., eds, Astronomical Society of the Pacific Conference Series Vol. 369, New Solar Physics with Solar-B Mission. p. 99

Pipin V. V., 2008, Geophysical and Astrophysical Fluid Dynamics, 102, 21

Pipin V. V., 2013, in Solar and Astrophysical Dynamos and Magnetic Activity Proceedings IAU Symposium No. 294. in press: arXiv1211.2426

Pipin V. V., Kosovichev A. G., 2011a, ApJ, 738, 104

Pipin V. V., Sokoloff D. D., Zhang H. et al. 2013, ApJ, in press. arXiv: 1211.2420P

Pipin V. V., Kosovichev A. G., 2011b, ApJ, 741, 1

Pipin V. V., Kosovichev A. G., 2011c, ApJL, 727, L45

Pipin V. V., Sokoloff D. D., 2011, Physica Scripta, 84, 065903

Pipin V. V., Sokoloff D. D., Usoskin I. G., 2012, A & A, 542, A26

Rädler K.-H., 1969, Monats. Dt. Akad. Wiss., 11, 194

Schrinner M., 2011, A & A, 533, A108

Seehafer N., 1990, Sol.Phys., 125, 219

Sokoloff, D., Bao, S., Kleeorin, N. et al., 2006, Astron. Nachr., 327, 876

Stix M., 2002, The Sun: An Introduction, Berlin : Springer

Usoskin I. G., Sokoloff D., Moss D., 2009, Sol.Phys., 254, 345

Vainshtein S. I., Kitchatinov L. L., 1983, Geophys. Astrophys. Fluid Dynam., 24, 273

Warnecke J., Brandenburg A., Mitra D., 2011, A & A, 534, A11

Woltjer L., 1958, Proc. Nat. Acad. Sci., 44, 833

Xu H., Gao Y., Popova E. P. et al. 2009, Astronomy Reports, 53, 160

Yoshimura H., 1975, ApJ, 201, 740

Zhang H., Moss D., Kleeorin N. et al. 2012, ApJ, 751, 47

Zhang H., Sakurai T., Pevtsov A. et al. 2010, MNRAS, 402, L30

## APPENDIX

Here we describe some details of the dynamo model that can be also fond in (Pipin et al. 2012; Pipin 2013)) and (Pipin 2008)(hereafter P08). The hydrodynamic part of the tensor $\alpha_{ij}$ is represented by $\alpha_{ij}^{(H)}$ (P08):

$$
\begin{aligned}
\alpha_{ij}^{(H)} &= \delta_{ij} \left\{ 3\eta_T \left( f_{10}^{(a)} \left( \boldsymbol{e} \cdot \boldsymbol{\Lambda}^{(\rho)} \right) + f_{11}^{(a)} \left( \boldsymbol{e} \cdot \boldsymbol{\Lambda}^{(u)} \right) \right) \right\} (11) \\
&+ e_i e_j \left\{ 3\eta_T \left( f_5^{(a)} \left( \boldsymbol{e} \cdot \boldsymbol{\Lambda}^{(\rho)} \right) + f_4^{(a)} \left( \boldsymbol{e} \cdot \boldsymbol{\Lambda}^{(u)} \right) \right) \right\} \\
&+ 3\eta_T \left\{ \left( e_i \Lambda_j^{(\rho)} + e_j \Lambda_i^{(\rho)} \right) f_6^{(a)} \right. \\
&+ \left. \left( e_i \Lambda_j^{(u)} + e_j \Lambda_i^{(u)} \right) f_8^{(a)} \right\},
\end{aligned}
$$

where, $\boldsymbol{\Lambda}^{(\rho)} = \boldsymbol{\nabla} \log \overline{\rho}$ is the inverse density stratification height, $\boldsymbol{\Lambda}^{(u)} = \frac{1}{2} \boldsymbol{\nabla} \log \left( \eta_T^{(0)} \right)$ is the same for the turbulent diffusivity, $\boldsymbol{e} = \boldsymbol{\Omega} / |\boldsymbol{\Omega}|$ is a unit vector along the axis of rotation. The turbulent pumping, $\gamma_{ij}^{(\Lambda)}$, depends on mean density and turbulent diffusivity stratification, and on the Coriolis number $\Omega^* = 2\tau_c \Omega_0$ where $\tau_c$ is the typical convective turnover time and $\Omega_0$ is the global angular velocity. Following the results of P08, $\gamma_{ij}^{(\Lambda)}$ is expressed as follows:

$$
\begin{aligned}
\gamma_{ij}^{(\Lambda)} &= 3\eta_T \left\{ f_3^{(a)} \Lambda_n^{(\rho)} + f_1^{(a)} \left( \boldsymbol{e} \cdot \boldsymbol{\Lambda}^{(\rho)} \right) e_n \right\} \varepsilon_{inj} \qquad (12) \\
&- 3\eta_T f_1^{(a)} e_j \varepsilon_{inm} e_n \Lambda_m^{(\rho)} \\
&- 3\eta_T (\varepsilon - 1) \left\{ f_2^{(a)} \Lambda_n^{(u)} + f_1^{(a)} \left( \boldsymbol{e} \cdot \boldsymbol{\Lambda}^{(u)} \right) e_n \right\} \varepsilon_{inj}.
\end{aligned}
$$

The effect of turbulent diffusivity, which is anisotropic due to the Coriolis force, is given by:

$$
\eta_{ijk} = 3\eta_T \left\{ \left( 2 f_1^{(a)} - f_2^{(d)} \right) \varepsilon_{ijk} - 2 f_1^{(a)} e_i e_n \varepsilon_{njk} \right\}. \qquad (13)
$$

We also include the nonlinear generation effects which is induced by the large-scale current and the global rotation that is usually called as the $\Omega \times J$ effect or the $\delta$ dynamo effect (Rädler 1969). It is supported by the numerical simulations (Käpylä et al. 2008; Schrinner 2011). P08 suggested that:

$$
\eta_{ijk}^{(\delta)} = 3\eta_T C_\delta f_4^{(d)} e_j \left\{ \tilde{\varphi}_7^{(w)} \delta_{ik} + \tilde{\varphi}_2^{(w)} \frac{\overline{B}_i \overline{B}_k}{\overline{B}^2} \right\}, \qquad (14)
$$

where, $C_\delta$ measures the amplitude of the $\Omega \times J$ effect, $\tilde{\varphi}_{2,7}^{(w)} (\beta)$ are normalized versions of the magnetic quenching functions $\varphi_{2,7}^{(w)}$ given in P08. They are defined as follows, $\tilde{\varphi}_{2,7}^{(w)} (\beta) = \frac{5}{3} \varphi_{2,7}^{(w)} (\beta)$. The last term in Eq.(14) is the nonlinear contribution to the $\Omega \times J$-effect. Its structure is the same as for the $\alpha$ effect because the associated electromotive force is proportional to $\frac{3}{2} \eta_T C_\delta f_4^{(d)} \tilde{\varphi}_2^{(w)} \overline{B}_i \left( \boldsymbol{e} \cdot \boldsymbol{\nabla} \right) \log \overline{\mathbf{B}}^2$ (see details in P08). Thus this effect works similar to the $\alpha$ effect that is excited by the nonlinear buoyant instability of large-scale magnetic field. The functions $f_{\{1-11\}}^{(a,d)}$ in Eqs(13) depend on the Coriolis number. They can be found in P08 (see also, Pipin & Kosovichev 2011b; Pipin & Sokoloff 2011).

The mixing-length is defined as $\ell = \alpha_{\mathrm{MLT}} \left| \Lambda^{(p)} \right|^{-1}$, where $\Lambda^{(p)} = \boldsymbol{\nabla} \log \overline{p}$ is the inverse pressure variation height, and $\alpha_{\mathrm{MLT}} = 2$. The turbulent diffusivity is parameterized in the form, $\eta_T = C_\eta \eta_T^{(0)}$, where $\eta_T^{(0)} = \dfrac{u'^2 \tau_c}{3 f_{ov}(r)}$ is the characteristic mixing-length turbulent diffusivity, $\ell$ is the typical

correlation length of the turbulence, $C_\eta$ is a constant to control the efficiency of large-scale magnetic field dragging by the turbulent flow. Also, we modify the mixing-length turbulent diffusivity by factor $f_{ov}(r) = 1 + \exp\left(50\left(r_{ov} - r\right)\right)$, $r_{ov} = 0.725R_\odot$ to get the saturation of the turbulent parameters to the bottom of the convection zone. The latter is suggested by the numerical simulations (see, e.g., Ossendrijver et al. 2001, 2002; Käpylä et al. 2008). The results do not change very much if we apply $\boldsymbol{\Lambda}^{(u)} = C_v \boldsymbol{\nabla} \log\left(\eta_T^{(0)}\right)$ with $C_v \leqslant 0.5$. For the greater $C_v$ we get the steady non-oscillating dynamo which is concentrated to the bottom of the convection zone. The purpose to introduce the additional parameters like $C_v = 0.5$ and $f_{ov}(r)$ is to get the distribution of the $\alpha$ effect closer to the result obtained in the numerical simulations.

The bottom of the integration domain is $r_b = 0.715R_\odot$ and the top of the integration domain is $r_e = 0.99R_\odot$. The choice of parameters in the dynamo is justified by our previous studies (Pipin & Kosovichev 2011a), where it has been shown that solar-types dynamos can be obtained for $C_\alpha/C_\delta \geqslant 2$. In those papers we find an approximate threshold $C_\alpha \approx 0.03$ for a given value of diffusivity dilution factor $C_\eta = 0.05$. The latter was chosen to tune the solar cycle period.